Faculty of Physics

University of Helsinki

MODERN ULTRASONICS: FROM SUPER-RESOLUTION LENS DESIGN TO INTRAOCULAR PRESSURE TESTER

Daniel Veira Canle

DOCTORAL DISSERTATION

To be presented for public discussion with the permission of the Faculty of Physics of the University of Helsinki, in Auditorium U3032, University Main Building, on the 24th of February 2023 at 12 o'clock.

Helsinki 2023

ISBN 978-951-51-8950-9 (Print)
ISBN 978-951-51-8951-6 (Online)

Unigrafia
Helsinki 2023

To my daughter who was born at the completion of my PhD and gave me the strength to take the final steps.

Abstract

The aim of this thesis is to lay the foundation for the development of a contactless laser-based tonometer. Tonometers are devices capable of measuring intraocular pressure (IOP). Monitoring intraocular pressure is important for diagnosing glaucoma, which is a disease that may result in blindness and affects 70 million people worldwide. The foundation behind the development of the proposed tonometer, rests on four published papers.

In the first paper we focused acoustic waves using cylindrical metamaterial lenses. These lenses allow focusing acoustic energy into a beam narrower than half the central wavelength of the wave package. By selecting the speed of sound ratio between the material inside the lens and the surrounding medium, as well as the lens diameter, it is possible to efficiently focus acoustic energy into a jet narrower than half the central wavelength. The generation of said jet involves the focusing of the narrow-bandwidth acoustic waves as they impinge on the lens. The lens' cylindrical geometry allows the propagation of guided surface waves on its structure that tailor the shape of the jet. An alternative approach towards generating a narrow acoustic wave front is the use of a pinhole. A pinhole in an aluminum plate allowed us to direct a shock wave front to a phantom/eye and calculate the intraocular pressure (IOP) from the time-of-flight of the membrane waves.

To detect these membrane waves, we used a laser Doppler vibrometer (LDV). The reason for using an LDV is that it allows contactless measurement of propagating membrane waves in the cornea. Avoiding contacting the cornea is important to prevent spreading pathogens and to retain patient comfort during the measurement. To understand the challenges of interferometric measurement with an LDV we conducted a study where we mapped the acoustic field on a rotating propeller. The motivation of this study was the importance of quickly monitoring the structural integrity of propellers *in situ* for the safe operation of aircraft. Aircraft inspection by ultrasonic means typically involves contacting transducers featuring low spatial resolution. Alternatively, laser ultrasonics allows fast characterization of materials with high spatial resolution and in a contactless manner. The demonstration of the contactless approach detected a flaw on an aluminum propeller that rotated under stroboscopic illumination of a high-power Q-switched laser. The high-power laser generated acoustic waves that travelled through the material and their measurement by an LDV resulted in acoustic maps. The maps allowed

the identification as well as the reconstruction of the defect on a 3D model of the sample.

We further increased the complexity of the sample from a planar propeller to a geometry closer to a human eye, a metal hemisphere. The complexity introduced by the curvature of the sample ranged from the difficulty of focusing an LDV on a curved target to acoustic resonances in the sample. The motivation for choosing these samples was to develop a method to inspect acetabular implants in a contactless manner. In a similar fashion to the propeller study, a metal hemisphere featuring a defect rotated whilst a high-power laser generated acoustic waves. The detection of these acoustic waves and mapping of the acoustic fields allowed a reconstruction of the defect on a 3D model of the hemisphere.

Further increasing the complexity of the sample, we studied an ocular phantom (human eye model) as a first step before measuring porcine eyes. In the phantom, the cornea was simulated by a polymer membrane stretched over a water-filled cavity. Adding water to the cavity increases the tension of the membrane and that is equivalent to increasing the intraocular pressure (IOP). To determine the internal pressure of the phantom, an electrical spark generated a shock wave that impinged on the phantom generating membrane waves. These waves propagated in the membrane and an LDV measured their amplitude and propagation time. By relating the time-of-arrival of the acoustic waves to the internal pressure of the phantom we extracted a calibration curve. We further expanded our database by measuring porcine eyes allowing us to compare the IOP readings of our method to those of the leading rebound tonometer, the iCare TA01.

The development of a contactless alternative to rebound tonometers will benefit from localized actuation on the cornea by a focusing structure, such as a metamaterial lens. Such a lens would allow actuation on a predetermined spot of the cornea, thus decreasing the uncertainty of the time-of-flight estimation. Such an uncertainty would be further reduced by eye tracking such that the excitation and detection locations remain fixed. The measurement series on the propeller introduces a method for synchronizing the excitation and generation of guided waves which is further improved in the study of the metal hemisphere. An important difference between eyes and metal hemispheres is the anisotropy of the tissue. Such anisotropy introduces variations in the acoustic impedance thus modifying the propagation velocity of membrane waves propagating in the cornea. Localized guided excitation of membrane waves would aid by launching guided waves along identical paths, thus decreasing the error in the estimation of the IOP.

The combination of the lessons learned together with eye-safe interferometric detection of guided waves might pave the way to safe and comfortable alternatives to the current tonometric methods.

Acknowledgements

The research contained in this thesis is based on the work carried out at the Electronics Research Laboratory, Department of Physics, University of Helsinki. I acknowledge Antti Kontiola for providing financial support for my PhD, as well as a wealth of medical and hands-on-knowledge about tonometer design. I thank Professors Edward Hæggström and Ari Salmi for their supervision and feedback on both my academic trajectory and publications.

I am deeply grateful to Timo Rauhala and Kalle Hanhijärvi for their support in the project to develop the tonometer. They introduced me to electronics design, testing and debugging as well as carrying out the measurements. Thank you, Tor Paulin, for the lengthy discussions about electronics design and the wealth of knowledge that you share willingly. My sincere thanks to my colleagues Henri Malinen and Peetu Ihalainen for their diligent work and support when further developing the contactless tonometer. Thank you, Joni Mäkinen for your diligence carrying out FEM simulations and for your support by sharing your physics knowledge and feedback. Thank you, Maria Gritsevich, for the tea-time discussions that evolved into publication III.

My sincere thanks to Axi Holmström, Fabio Valoppi, and Joni Mäkinen for reading the final draft of this thesis and providing feedback. Your physics knowledge, and pursuit for coherent writing have sharpened up this work.

Lastly, I would like to thank my wife for her support. Thank you for being there every day and encouraging me to move forward. Thank you for speaking up about my limitations as a writer, and for suggesting literature to develop my writing skills. This single fact allowed me to ditch everything I knew about writing, rewrite publication III, and have it accepted.

Daniel Veira Canle, February 2023, Helsinki

Contents

List of original publications

This thesis is based on the following publications:

I) Veira Canle, D. et al. Practical realization of a sub-λ/2 acoustic jet. *Sci. Rep.* **9**, (2019).

II) Veira Canle, D., Salmi, A. & Hæggström, E. Non-contact damage detection on a rotating blade by Lamb wave analysis. *NDT E Int.* **92**, (2017).

III) Veira Canle, D. *et al.* Defect localization by an extended laser source on a hemisphere. *Sci. Reports 2021* **11**, (2021).

IV) Salmi, A., Nieminen, H. J., Canle, D. V., Hæggström, E. & Kontiola, A. Non-contact determination of intra-ocular pressure in an ex vivo porcine model. *PLoS One* **15**, e0227488 (2020).

The publications are referred to in the text by their roman numerals.

Author's contributions:

In contribution I, the author assisted in building the measurement system, performed the measurements and carried out the data analysis. The author helped writing the first draft of the manuscript and contributed to finalizing it for publication. In contribution II, the author developed the experiments, built the experimental setup, carried out the measurements, analyzed the data, wrote, reviewed, and edited the publication. In contribution III, the author planned and executed the experiments, analyzed the experimental data, derived the equations, wrote, reviewed, and edited the publication. In contribution IV, the author assisted in the analysis of the data as well as its visualization, helped writing, reviewing, and editing the publication.

Abbreviations

IOP	Intraocular Pressure
LDV	Laser Doppler Vibrometer
CMOP	Custom-Made Ocular Phantom
FEM	Finite Element Method
MD	Molecular Dynamics
λ	wavelength
FWHM	Full Width at Half Maximum
Nd:YAG	Neodymium-Doped Yttrium Aluminum Garnet

1 Introduction

Monitoring intraocular pressure (IOP) is crucial to diagnose glaucoma, a disease affecting over 70 million people worldwide [1] with a cost of $1.9 billion in the United States alone [2]. Patients find current state-of-the art tonometers ranging from applanation and air-puff methods to rebound tonometers uncomfortable since most of them exert pressure on the eye.

The current gold standard in IOP measurement and monitoring is the Goldmann applanation tonometer. The main advantage of such an approach is that the method is widely available and well established. On the down side, topical anesthesia is required as IOP is estimated by measuring the deflection of a pin pushing the cornea with the possibility of subsequent corneal damage [3].

In contrast, rebound tonometry utilizes the dynamics of a probe contacting the cornea to estimate the IOP [4], [5]. The current state-of-the art of rebound tonometry is the iCare tonometer. The main advantage over Goldmann that is measurements do not require local anesthesia [6] and that probes are disposable thus minimizing the risk of cross-contamination. Nevertheless, contacting the eye renders this method uncomfortable to some patients further demonstrating the need for a contactless tonometer.

Air-puff tonometry is a contactless method based on the applanation of the cornea by a puff of air. A light emitter and receiver are placed coaxially at a fixed angle with respect to the corneal apex. When the cornea is flattened the light beam is no longer coaxial and the amount of time required for applanation is measured. There is a direct relation between deflection time and IOP with longer time intervals indicating higher IOP [7]. Measuring the IOP does not require the use of anesthesia and there is no risk of corneal abrasion [8]. Some of the downsides of air-puff tonometry are that the puff of air can startle some patients, and the generation of aerosols by the air jet. The aerosols can potentially spread pathogens such as bacteria and viruses [3] [8] [9]. By comparison, the IOP values estimated by air-puff tonometry are typically higher than those measured with Goldmann. As a result, the

Goldmann applanation tonometer has remained the gold-standard to this day [8].

To develop a contactless tonometer that might substitute the gold standard, we excite with an airborne shock wave a membrane wave that travels on the surface of the cornea. Restricting the excitation footprint to an area with a width smaller than the acoustic wavelength of the membrane wave (λ) is crucial for the effective generation of guided waves on the cornea. In practice we restricted the footprint of the shock front by means of an aluminum plate featuring a hole smaller than the wavelength of the membrane wave. The generation of a narrow acoustic spot is possible by modifying the numerical aperture of the sound emitter, using subwavelength structures such as antennas, and using metamaterial lenses [10].

We demonstrated how to build such a lens for an immersion setup, carried out experiments and performed finite element methods (FEM) and molecular dynamic (MD) simulations from macroscale (cm-mm) to nanoscale (μm-nm). Both in the experiments and simulations, we chose a refractive index ratio for the metamaterial lens close to 1.7 and a container featuring a diameter ranging from 20 to 30 wavelengths (wavelength of the sound propagating in the surrounding medium). Such metamaterial lens dimensions ensure that the lens acts as a macroscopic object where waves circulating on the container walls, and longitudinal waves travelling through the lens filling combine to generate an acoustic jet (paper I). The choice of refractive index ratio follows the methods established by Chen [11] to generate a photonic jet in the optics domain, and the motivation for the approach is based on our experience with photonic jets [12].

Jets would restrict the footprint of the excitation in a tonometric application. Alternatively, one could reduce the size of the acoustic source itself. Such a feat has been achieved with lasers by means of a plasma spark for the generation of guided waves [13]. Laser generation of acoustic waves mainly operates in two regimes: thermoelastic and ablative. In the thermoelastic regime a laser momentarily heats up a region of the sample's surface creating a temperature gradient and thermal expansion. The thermal expansion results in stress propagation and the generation of guided waves [14]. The amplitude of these guided waves is small (few hundred picometers [13]) resulting in low signal-to-noise ratio as compared to contacting techniques. Furthermore, the laser absorption depends on the absorbance of the sample's surface, which may vary depending on *e.g.,* its cleanliness and roughness. Alternatively, one can operate in the ablation mode; when the laser fluence surpasses $10^{12} - 10^{14}\ Wm^{-2}$[15]–[22]. In this case, the excitation laser ablates the material, and

the plasma plume generates a reactive force that induces guided waves. However, the surface of the sample is modified for every laser pulse which results in unpredictable wave forms and in week spots, where cracks might initiate in the future. Further increasing the fluence of the laser, it is possible to generate breakdown of air just above the surface of the sample. In this way, a high signal-to-noise ratio is obtained in a non-destructing manner. In addition, the excitation of guided waves does not depend on the surface absorbance as in the thermoelastic case, thus combining the best of both thermoelastic and ablative excitation [14], [21]. Laser-induced air breakdown could provide consistent membrane wave generation on the cornea and in combination with interferometric detection of membrane waves could become a contactless approach to measure IOP.

Eyes are challenging samples to measure by laser interferometry. The laser beam must be perpendicular to the surface of the sample to measure the out-of-plane wave amplitude. In addition to the measurement difficulties, curved geometries introduce challenges for acoustic waves that are absent in planar geometries including geometric focusing, presence of resonances, curvature-induced dispersion, and multipath interference [14], [23]–[26]. These issues motivated a laser ultrasonic study, where we localized a defect on metal hemispheres by means of directed guided acoustic waves. To generate directivity of the acoustic field, we shaped the laser excitation to a line. Shaping the laser acoustic source both in time and space is a well-known technique that allows tailoring of the acoustic wave profile [27]–[30]. The achieved directionality improved the image contrast by avoiding spurious echoes, allowing us to identify echoes from the defects and to reconstruct the defects on a 3D model of a hemisphere.

In addition to the challenges introduced by the spherical geometry of the eyes, when measuring patients, synchronization of the excitation and detection of the membrane waves is key. We tackled a similar synchronization problem when we developed a stroboscopic method to inspect rotating propellers by means of laser ultrasound. The aim of the laser ultrasonic approach was to localize a defect in a contactless manner on a rotating aluminum blade. In contrast to current inspection methods used in the aviation industry [31], our approach could allow in-situ inspection of rotating propellers in the field.

Damage localization performed with laser ultrasound circumvents many limitations present when one employs conventional contact transducers [14]. Coupling transducers to curved geometries is nontrivial, since they must match the sample shape. Furthermore, the transducer causes mass loading onto the surface of the sample, which modifies the boundary conditions for

wave propagation resulting in a distorted waveform [14]. Acoustic wave generation and detection with lasers allows fast scanning of moving samples with high resolution, even when direct access is restricted.

In addition to the aforementioned advantages over contacting techniques, for this application, laser ultrasound is superior to other contactless inspection methods. Both thermal and eddy current imaging cannot detect buried defects and these techniques are limited to heat [32]–[34] or electrically conductive samples [35]–[39]. X-ray imaging is often used to inspect large structures in aviation as it can scan samples with high resolution. X-rays are nevertheless limited to inspection of static structures requiring propellers to be removed for inspection [40]–[42]. Something worth noting is that ultrasound is very versatile, and it is not limited to aviation. Ranging from medical ultrasonography [43] to ultrasonic cleaning [44], and the study of the mechanical properties of materials [45] the applications of ultrasound are broad. Of particular interest is the use of lasers for the measurement of acoustic wave forms. Undistorted wave forms can only be achieved with point-like measurements of the acoustic field and focusing a laser tighter the acoustic wavelength guarantees signal fidelity [14].

The high spatial resolution of the laser interferometer allows determining the time-of-arrival of generated waves with high temporal accuracy, because the detection point is well-defined, small and stable. The approach is similar to acoustic-microtapping where guided waves generated by air-coupled ultrasound propagate along the cornea and are observed by optical coherence tomography (OCT) [46]. The main difference is that a shock wave produces a broadband excitation generating surface waves that travel from the edge of the eye towards the apex of the cornea, where a laser Doppler vibrometer (LDV) detects their passing. The travel time of the guided waves depends on the IOP. We first verified this hypothesis be means of an ocular phantom and we later calibrated the setup using excised porcine eyes.

When extrapolating the foundation from this work to the measurement of human eyes, it will be paramount to safely generate a directed membrane wave in the cornea. Eye tracking would ensure that membrane waves are generated and detected similar locations in successive measurements, reducing the error induced by differences in the time-of-flight of the propagating waves. Such an approach would allow gathering enough data to reduce measurement error and develop a tonometer that might in the future substitute the gold standard.

2 Methods

2.1 Samples and topology of the study

To acquire wave forms with a narrow temporal distribution localizing the shock wave front to a small region on the surface of the eye is crucial. Focusing of acoustic energy into a region with a width smaller than $\lambda/2$ is possible with metamaterial lenses across a wide range of length scales. In the millimeter and micrometer scales we performed FEM simulations (COMSOL Multiphysics® v. 5.2) and experiments. In both these cases, we simulated a lens filled with perfluorinated oil immersed in water, olive oil, and ethanol. We chose water and olive oil because they are biocompatible and ethanol because the speed of sound ratio perfluorinated oil-ethanol guarantees subwavelength acoustic focusing.

We studied the scalability of the method to understand how small a metamaterial lens can be while effectively focusing acoustic energy. To focus acoustic energy into a narrow region, we selected materials with an acoustic refractive index ratio of 1.7 and we scaled down the size of the metamaterial lens. In the micrometer range, a gold metamaterial lens embedded in nickel was also studied with FEM simulations and in all cases the simulations ran in the frequency domain in a 2D geometry with a pressure boundary condition at the bottom and enclosed by perfectly matched layers.

Further scaling down into atomic scale, MD simulations (LAMMPS) allowed us to study the focusing properties of a germanium cylinder (28 nm) embedded in silicon (114x114x2.2 nm^3). To minimize the effect of lattice mismatch, we modified the model so that the lattice spacing for silicon was the same as for germanium. Following the potential model introduced by Balamane and Laradji [47], [48] we minimized the potential energy of the system (at zero Kelvin) and launched a Gaussian plane wave ($5x10^{-4}$nm amplitude, FWHM of 7 ps) into the silicon matrix.

The experimental setup consisted of a cylindrical vial filled with perfluorinated oil that was inserted into a 3D-printed tank (paper I, Fig. 7). An acrylic block attached to the tank ensured that the acoustic waves launched by a transducer (Karl Deutsch S24 HB 0.3-1.3 MHz) were plane waves. These waves were

detected by a hydrophone (200 μm thick probe, SN2151 precision acoustics) that was moved by a translation stage. To perform a scan, first we lowered the translation stage until it gently touched the surface of the lens, then retracted the probe 100 μm and scanned the transversal plane to the lens (xz plane) in lateral steps of 100 μm and heigh steps of 50 μm. At each point the transducer launched an ultrasonic burst (5 cycles, 430 kHz, 164 V peak-to-peak amplitude) whose resulting acoustic waveforms we integrated over two cycles resulting in the acoustic maps.

The measurement of acoustic maps requires a stroboscopic approach in moving samples. Two bow tie shaped aluminum blades (130x75x4 mm^3) allowed us to develop a contactless method for localizing defects in a rotating propeller (paper II) (Fig.1). One of the samples was pristine and the other featured a cavity 5x10x2.4 mm^3 in size located at 35.10 mm from the center of the sample. The propellers rotated under illumination by a Q-switch Nd:YAG laser (CFR Big Sky Series, 8 ns, 189 mJ, 1.2 Hz pulse repetition frequency) and an LDV (OFV303 laser head, OFV3001 controller, 2 MHz bandwidth in displacement mode, detection spot situated at 9.6 mm distance from the center of the sample) digitized the generated guided waves.

The information carried by these waves depends on the type of scan. A linear scan (Fig. 1a) probes the sample (232 points per scan, 80 measurements per point) lengthwise providing information about the dispersion curves of the guided waves, their group velocity as well as the width of the cavity and its distance from the center of the sample. The length and depth of the cavity was calculated from the information obtained from an arc scan. In this configuration (Fig 1b) the distance between the detection and excitation locations stays constant (32.6 mm) whilst the control software scans the sample in an arc. This approach launches guided waves that travel across the length of the defect allowing the calculation of said dimension. The cavity depth is calculated by knowing the group velocity of the waves travelling through the defect as well the dispersion curves of the waves propagating through the intact plate.

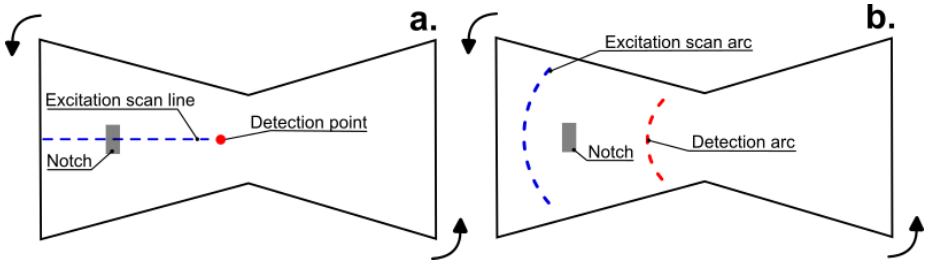

Figure 1 Comparison between a linear scan (a) and an arc scan (b). In the linear scan approach the Nd:YAG laser spot (blue) scans the sample from the edge towards the detection point (LDV, red). In the arc scan approach, the distance between the detection and the excitation stays constant. Here the computer synchronizes the measurements allowing the lasers to probe the sample in arcs.

Further increasing the complexity of the sample from a plate to a metal hemisphere, in paper III we measured hemispheres similar in size to acetabular implants (diameter 50 mm, 0.6 mm thickness). With these samples we developed a contactless method for localizing cavities on a curved geometry. We studied four different samples one was pristine and the other three featured cavities of sizes 8, 4.5 and 2 mm. These samples were rotated azimuthally (3 rotations at 200 steps per revolution) and a Q-switched Nd:YAG laser (CFR Big Sky Laser Series, 40 mJ per pulse, pulse duration 8 ns, 3 Hz pulse repetition rate, non-ablative regime) generated guided waves in the structure (Fig. 2). The directivity of the guided waves was adjusted by selecting a point or line source for the footprint of the excitation laser. To verify the laser experiments FEM simulation models (COMSOL Multiphysics® v. 5.3a) coupled the Heat Transfer Module to the Solid Mechanics Module. The combination generates thermal stresses in the time domain leading to elastic wave propagation. To recreate the experimental point and line acoustic sources, we modelled the geometry of the excitation as Boundary Heat Sources. These sources comprised two perpendicular Gaussian profiles where the FWHM was 1 mm in the case of the point source and 0.90 mm (line width) and 7.8 mm (line length) in the case of the line excitation. The simulations registered the acoustic waveforms generated by these excitation profiles at 1.85 mm distance from the edge of the sample.

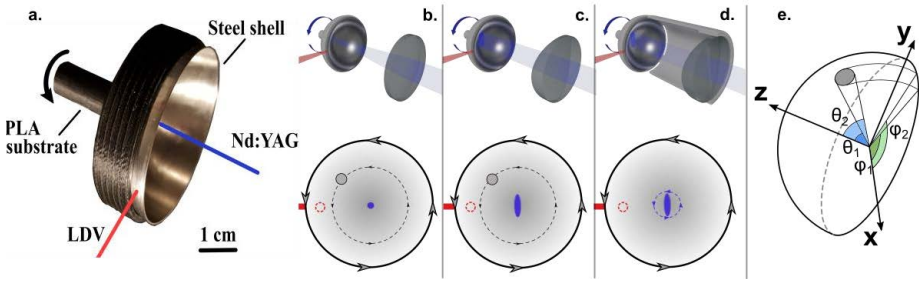

Figure 2 Experimental setup for localizing a cavity on a stainless-steel shell. The shell rotated under illumination by a pulsed Nd:YAG laser which generated guided waves that an LDV detected at 0.8 mm distance from the edge of the sample (a). To localize the cavity (gray circle, e), we compared two acoustic source geometries, a laser spot (b) and a line (c). We further characterized the acoustic directivity of the line source by probing the excitation with a cylindrical lens attached to the sample (d).

To calculate IOP, it is crucial to establish the relation between the propagation speed of guided waves and the IOP (paper IV). To build up confidence that the approach works before studying biological samples, we built an ocular phantom. The phantom comprised a cylindrical container, whose lid featured a thermoplastic polyurethane membrane (Fig. 3a). We adjusted the tension of the membrane by pumping liquid into the container through a silicone tube connected to a syringe. The induced tension was equivalent to IOP ranging from 18 to 40 mmHg, as measured by the iCare TA01 tonometer.

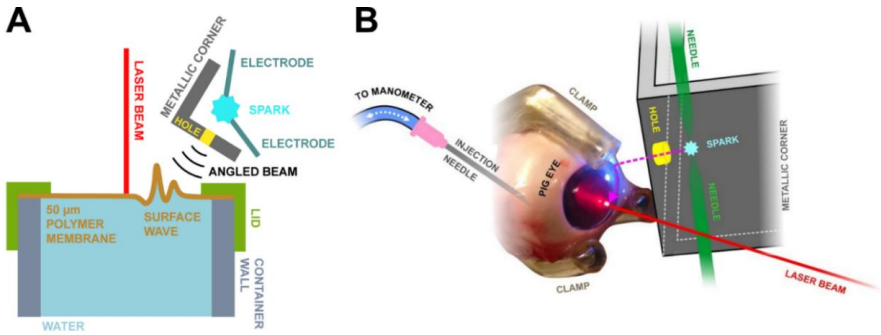

Figure 3 Measurement setup for the contactless measurement of intraocular pressure from an ocular phantom (a) and a porcine eye (b).

To validate the tonometric approach we developed an experimental setup to contactlessly measure the IOP of four porcine eyes. We pressurized these eyes with Phosphate-buffered saline solution (PBS, 0.01M) injected through a 18G needle (Fig. 3b) and monitored the IOP with a water column. We pressure-cycled three different eyes from 10 to 77 mmHg and to establish the repeatability of the method, we pressure-cycled one eye three times with pressures ranging from 10 to 70 mmHg.

Both in the pressure experiments carried out on the phantom and the eyes, a shock wave generated by an electric discharge (167 nF capacitance at 10 kV and 1 mm spark gap, Fig. 4) travelled through a 2 mm hole in an aluminum plate. The so confined excitation impinged on the sample (phantom or eye) located 15 mm away from the spark location generating guided waves. These waves were detected at the corneal apex by an LDV (sensor head: OFV-505, controller: OFV-2570) and the data was acquired by an oscilloscope (Lecroy WaveRunner, 100 million samples per second, 50 averages per signal).

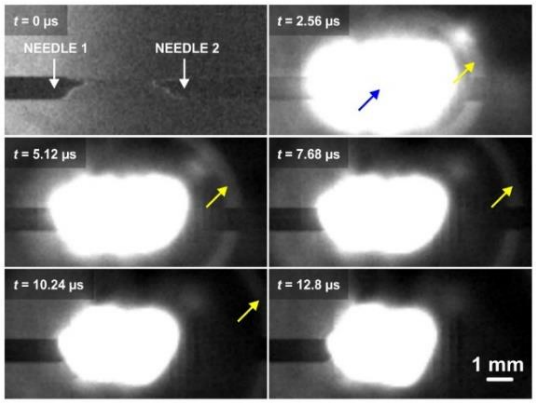

Figure 4 Schlieren image (frame rate 391,000 frames per second) of the shock wave (yellow arrow) generated by the electric discharge (167 nF at 10 kV across a 1 mm gap).

2.2 Data analysis

Performing an image reconstruction in paper II was challenged by a unique problem to rotating geometries; coherent noise introduced by fluttering (Fig. 5). We tackled the coherent noise problem by median filtering the data and averaging over three rotations allowing us to reconstruct the defect from the acoustic maps of the propagating guided waves.

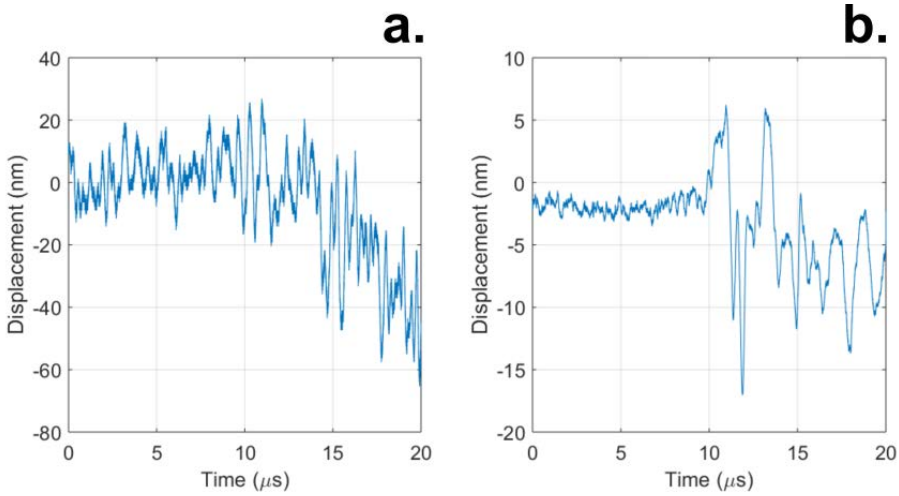

Figure 5 Comparison between a raw signal (a) and an 80-point-median-filtered signal (b). Median filtering removes coherent noise allowing the detection of the A0 mode arriving at 10μs.

In a similar manner to the research done in paper II, localizing a defect on a metal hemisphere with laser ultrasound requires averaging. Here (paper III) the samples rotated three times azimuthally (3 rotations at 200 steps per revolution) and a purpose-written MATLAB algorithm (MathWorks® R2018b) constructed acoustic maps by stacking the filtered signals (Fig. 6) (Butterworth high-pass filter, 62.47 MHz sampling frequency, 0.1 MHz stop frequency, and 0.5 MHz pass frequency) next to each other. This way it is possible to interpret echoes carrying information about the defect size and location that otherwise would have been buried by the resonance of the hemisphere at 120 kHz. After filtering, localizing the defect is straightforward from the time-of-flight of the A0 Lamb wave and its group velocity. We calculated the size of the defect from the -3dB points of the acoustic power (width) and the time-of-flight of the echoes reflected from the scatterer (length).

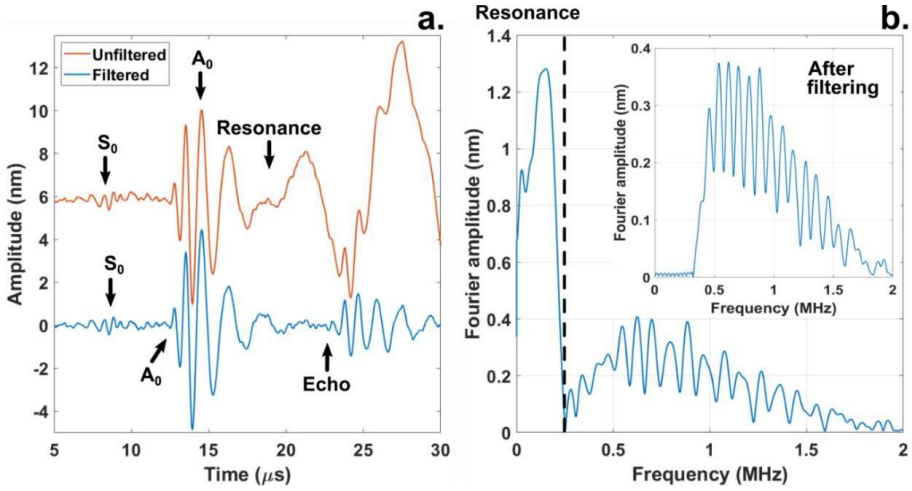

Figure 6 Filtering waveforms to remove resonances. Resonances naturally occur in confined structures (especially with broadband excitations), and they impede interpretation of echoes (a). A Butterworth high-pass filter with 0.1 MHz stop frequency and 0.5 MHz pass frequency effectively removes the resonance from the measured data.

Moving on to the tonometer study (paper IV), the time-of-flight estimation of membrane waves propagating in the phantom requires filtering of the measured data. Filtered data (Savitzky-Golay, 2000 points) from the custom-made ocular phantom (CMOP) experiments allowed us to develop the analysis algorithm (Matlab R2015a). A set comprised of fourteen signals measured at different IOPs established a database allowing us to calibrate the algorithm. Such a calibration was based on time-of-flight data of the propagating guided waves. We calculated the time-of-flight of the guided waves as the time difference between the excitation of the shock wave and the detection of the third positive peak of the wave form. We chose the third positive peak of the wave form since it is a clear feature in all the signals (Fig. 16). Fifteen

additional signals validated the calibrated algorithm in an exercise where the algorithm was blind to the measured IOP values.

We developed a similar algorithm (Matlab R2016a) to estimate the IOP from the porcine eye measurements. These measurements featured a different shape of the wave form, which required an alternative approach to calculate the time-of-flight. In this case, the algorithm automatically calculated the time-of-flight by finding the maximum of the envelope of the wave form. These wave forms required substantial filtering. In addition to the 2000-point Savitzky-Golay filtering, we filtered them with a 200-point moving median, a 120-point sliding average and an infinite impulse response Butterworth low-pass filter. We rejected several signals featuring poor signal-to-noise ratio and manually corrected gross time-of-flight estimation errors.

3 Results

Reconstructing defects on a model of the sample requires the measurement of the scattered acoustic field by the scatterer of interest (papers II, and III). The complementary of a scatterer, such as a hole or notch is a confined region that emits acoustic waves. One could consider the similar case in which an acoustic field travels through a small aperture compared to the wavelength of the guided waves in the sample. That was the case when developing a tonometer as we confined the shock wave excitation (Fig. 4) using an aluminum plate featuring a small hole compared to the wavelength of the resulting membrane waves.

Wave focusing into a region smaller than the diffraction limit is possible by launching acoustic waves into a cylindrical metamaterial lens (Fig. 7). We built a homogeneous metamaterial lens, whose filling featured a speed of sound lower than the surrounding medium, and focused acoustic energy into a subwavelength focal spot. The experimental results (Fig. 7,8, & 9) show that for a given frequency (Fig. 7 & 9), the width of the jet depends on the material inside the lens as well as on the distance to its surface.

We verified this result experimentally and in FEM simulations on macroscale and extrapolated the study to the microscale and nanoscale (Fig. 8e & c). FEM simulations show that by scaling down the size of the metamaterial lens, one can achieve subwavelength focusing on the microscale with the same materials as in the macroscale (Fig. 8d). Molecular dynamics (MD) simulations corroborate the FEM results in solids by showing that subwavelength focusing is possible in the microscale (Fig. 8e). Scaling down the study to nanoscale is possible and according to MD simulations a germanium metamaterial lens would allow subwavelength focusing in silicon (Fig. 8c).

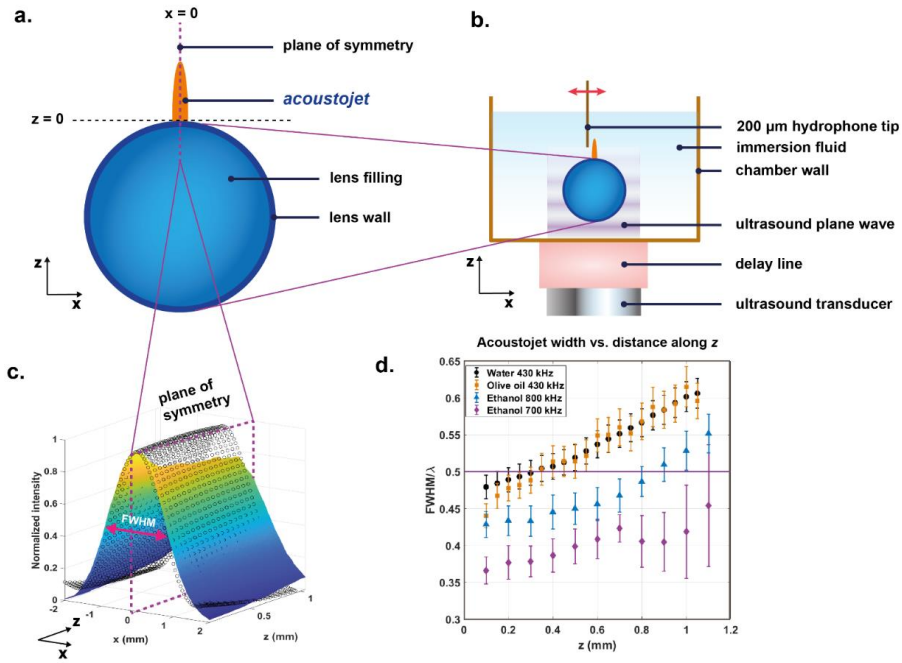

Figure 7 Focusing acoustic energy into a subwavelength acoustic sheet on the macroscale. The combination of an ultrasonic transducer and a delay line generate a plane wave that impinges on a metamaterial lens (a) generating an acoustic sheet in the surrounding fluid (b). Experiments and FEM simulations show that the sheet is symmetric about its plane of symmetry in water (c). Experiments show that other media, *e.g.* ethanol also exhibit subwavelength-wide acoustic focusing (d). The error bars feature confidence limits of one standard deviation.

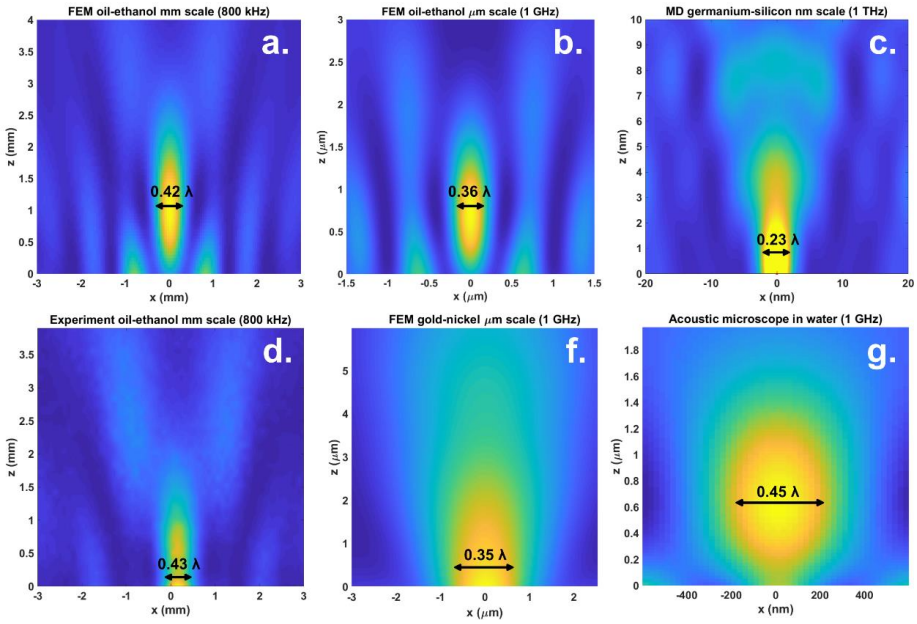

Figure 8 Focusing acoustic energy into sub $\lambda/2$ spots with metamaterial lenses. (a) FEM simulation on the macroscale verifies the experimental results (d) generated by an oil-filled lens immersed in ethanol. (b) FEM simulation featuring the same lens as in (a) and (d) but in microscale; (e) extrapolation of the FEM simulations in microscale to solids using a solid gold lens embedded in nickel. (c) MD simulation of a solid germanium lens embedded in silicon in nanoscale; (f) FEM simulation of a metamaterial lens dedicated for acoustic microscopy.

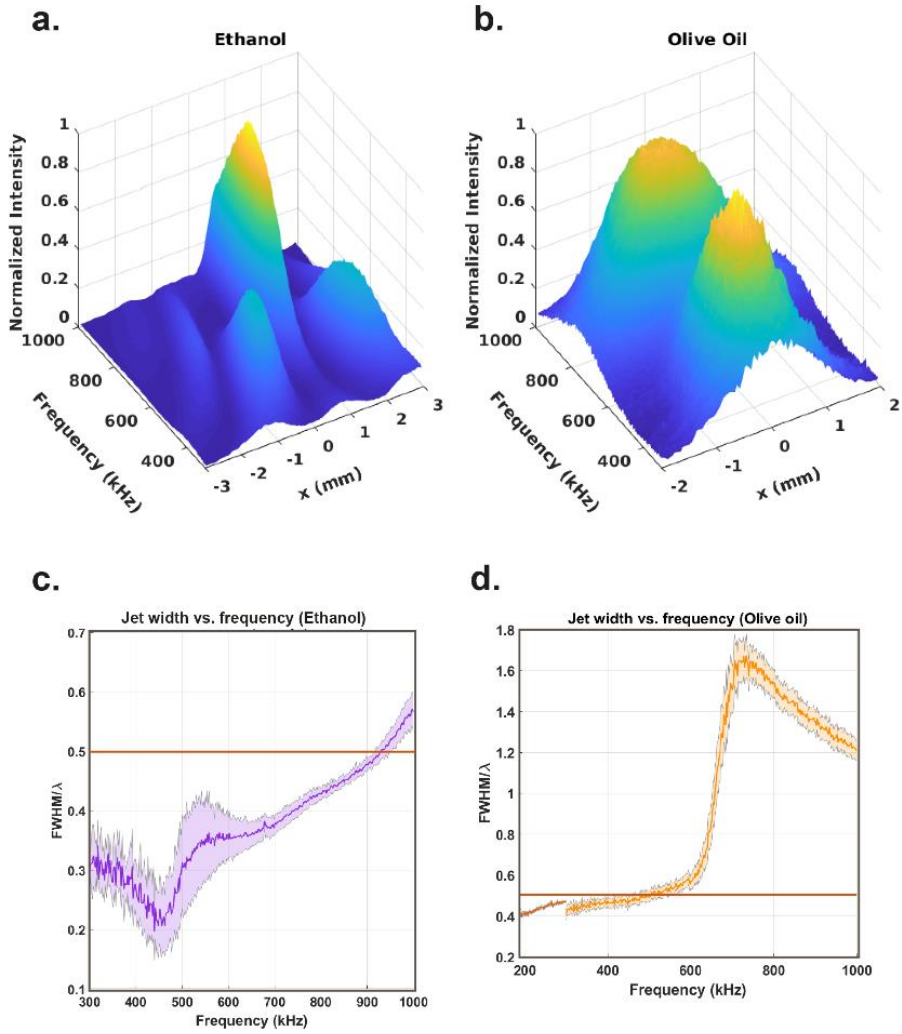

Figure 9 Acoustic jet profiles generated by metamaterial lenses filled with ethanol (a) and olive oil (b) as a function of lateral distance and frequency. The full width at half maximum (FWHM) of the acoustic jet changes with the ultrasonic frequency both in ethanol (c) and in olive oil (d). Here the pastel colors represent confidence limits of one standard deviation. The solid orange line marks the $\lambda/2$ line and the different orange colors in (d) represent two different ultrasonic transducers.

Material selection and sizing of the metamaterial lens based on the speed of sound ratios between the lens and the surrounding media, allows us to focus acoustic power on a confined region. Alternatively, one can tailor the acoustic energy distribution in the time domain e.g., by means of a stroboscopic approach. Such a stroboscopic approach times the excitation and detection of acoustic waves on a rotating target enabling the reconstruction of a defect on a 3D model of the sample (Fig. 10, Table 1).

Scanning the propeller longitudinally (line scan) provides information about the location and length of the defect (Fig. 11a to c). The width of the defect is calculated from an arc scan where the lasers scan the sample transversally (Fig. 11d to f). The arc scan shows the delayed A_0 mode (Fig. 11e, f), whose phase velocity is transformed, using the dispersion curves for Lamb waves (Fig. 12), into the depth of the defect.

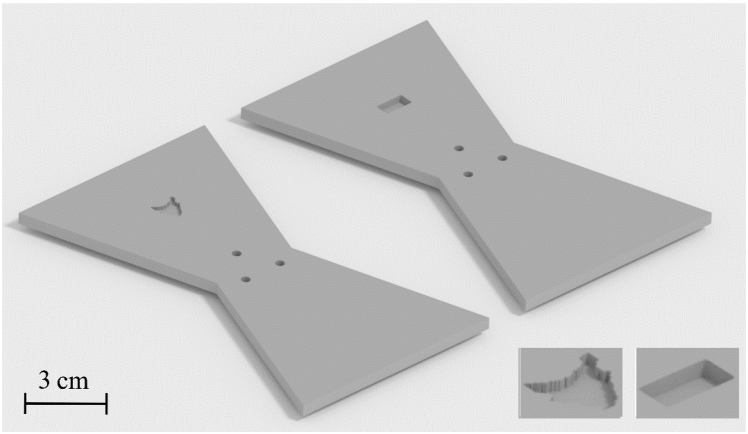

Figure 10 3D visualization of the flat propeller comparing the reconstructed defect (left) to the original sample (right).

	Estimated value (mm)	Expected value (mm)
Length (l)	5.7 ± 1.8	5
Width (w)	9.3 ± 0.9	10
Depth (D)	2.3 ± 1.0	2.4
Distance (d)	34.6 ± 2.2	35.1

Table 1 Pit dimensions and location obtained by the laser ultrasonic method compared to the expected values.

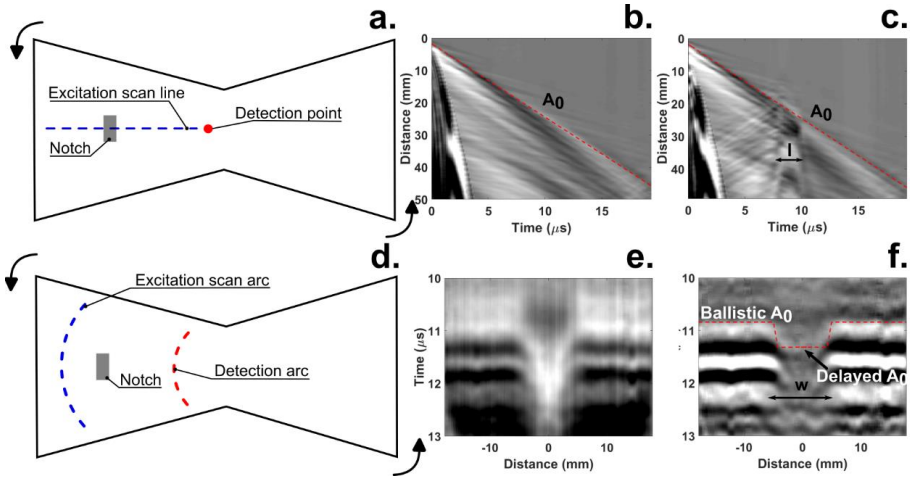

Figure 11 Top row: linear scan, bottom row: arc scan. Performing a linear scan along the length of the sample (a,c) and comparing the results to a scan of the pristine sample (b) allows the calculation of the location and length (l) of the defect. An arc scan (d) yields information about the width (w) and depth (D) of the defect after the A_0 waveforms (e) have been filtered (f).

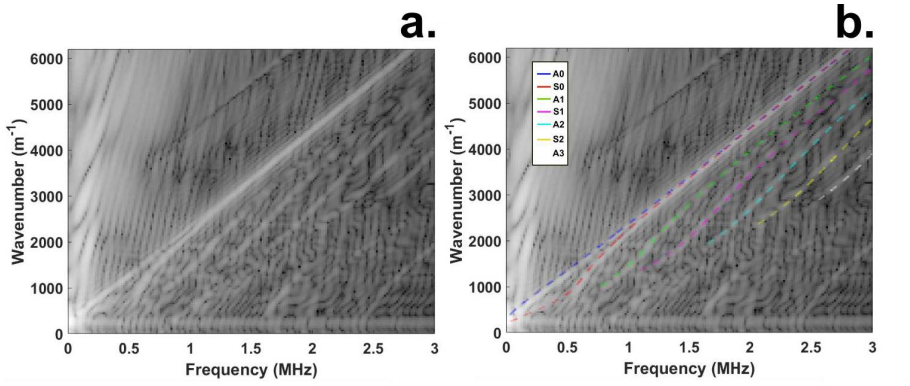

Figure 12 Experimental dispersion curves of Lamb waves travelling on the rotating propeller (a). Superimposing the curves corresponding to the Lamb wave modes verifies that the waves propagating in the sample are indeed Lamb waves (b). Using these curves, it is straightforward to calculate the depth of the defect from the propagation velocity of the A_0 mode.

Defect reconstruction in spherical geometries (paper III) (Fig. 13) required mapping the acoustic waves generated by laser excitation. We first positioned these lasers pointing at the equator at opposite ends of the hemisphere (Fig. 14). This approach, however, provides insufficient information to visualize the defect.

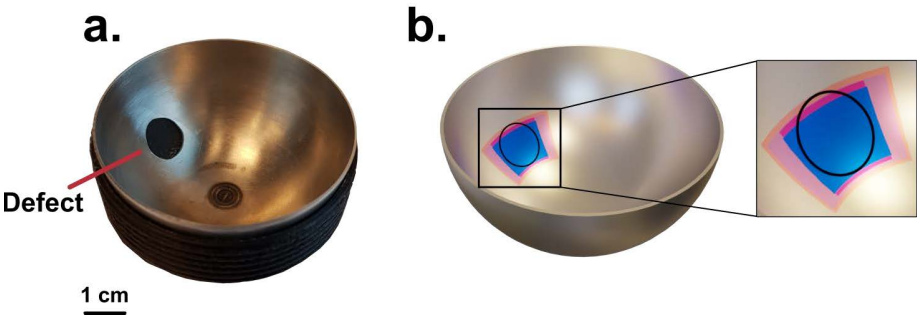

Figure 13 Visualization of a 9.5 mm cavity: Photograph of the sample featuring the detect (a). 3D CAD model of the sample (b). The black circle represents the expected size and location of the cavity. The dark red and dark blue sectors are the expected locations obtained from experiments and FEM simulations, respectively. The light red and light blue areas represent the confidence limits from the experimental and simulation approaches.

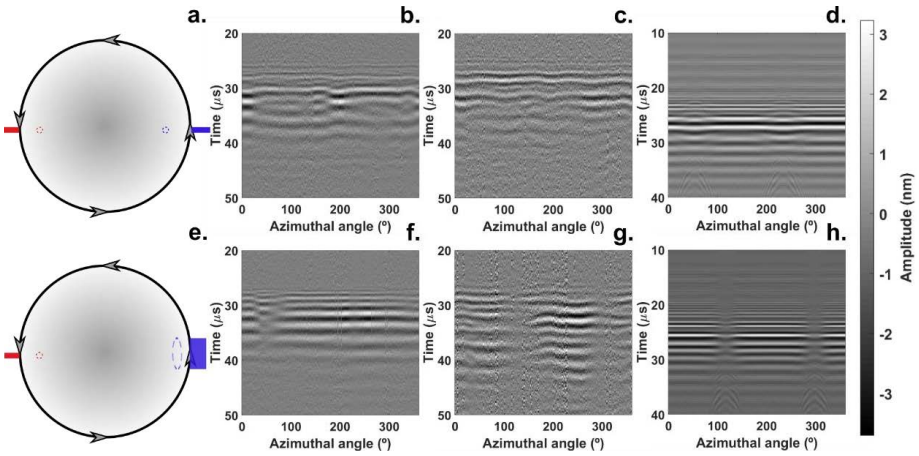

Figure 14 Side-to-side measurement of the stainless-steel hemisphere with laser ultrasound Top: point-source as a wave source. Bottom: line-source as a wave source. a,e: schematic representation; b,f: intact sample; c,g: sample featuring cavity; d,h: FEM simulation of a sample featuring a cavity.

Moving the excitation location to the zenith whilst keeping the detection at the equator of the hemisphere allowed us to obtain data from echoes radiating from the cavities (Fig. 15). This information allowed us to calculate the location of the defects and established the spatial resolution of the method (Table 2).

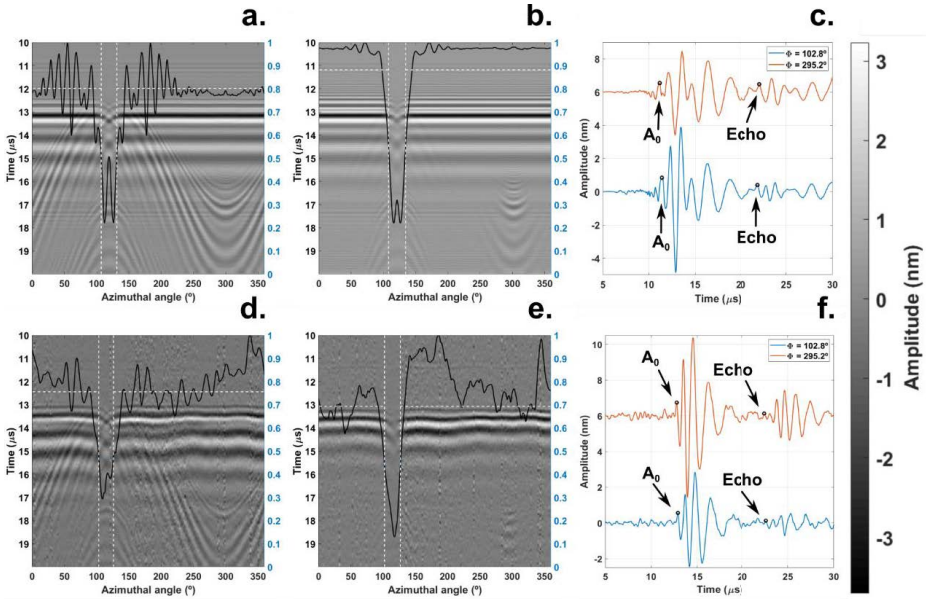

Figure 15 Results obtained with the acoustic source placed at the zenith and the detection location at the equator. Top row: FEM simulation results. Bottom row: experimental results. a,d: point source; b,e: line source; c,f: echoes at the azimuthal angles ϕ= 102.8° and ϕ=295.2° radiating from the defect.

9.5 mm defect		4 mm defect		2 mm defect	
Polar angles (°)					
55.74 ± 0.23	34.26 ± 0.23	49.58 ± 0.23	40.42 ± 0.23	47.29 ± 0.23	42.71 ± 0.23
56.2 ± 1.9	34.0 ± 1.9	52.2 ± 3.7	37.8 ± 3.7	49.4 ± 3.4	40.6 ± 3.4
55.2 ± 2.0	35.8 ± 2.0	50.2 ± 3.7	39.8 ± 3.7	49.0 ± 3.7	41.0 ± 3.7
Azimuths (°)					
105.99 ± 0.16	136.42 ± 0.16	114.72 ± 0.16	127.68 ± 0.16	117.96 ± 0.16	124.44 ± 0.16
102.0 ± 6.5	127.7 ± 6.5	115.9 ± 2.7	126.5 ± 2.7	-	-
108.0 ± 5.0	134.4 ± 5.0	114.0 ± 2.7	128.4 ± 2.7	110.2 ± 4.2	132.2 ± 4.2
Length, l (mm)	Width, w (mm)	Length, l (mm)	Width, w (mm)	Length, l (mm)	Width, w (mm)
9.39 ± 0.10	9.39 ± 0.10	4.00 ± 0.10	4.00 ± 0.10	2.00 ± 0.10	2.00 ± 0.10
9.7 ± 1.4	7.9 ± 2.8	6.3 ± 2.3	3.3 ± 1.2	3.8 ± 2.1	Not visible
8.5 ± 1.4	8.2 ± 2.2	4.2 ± 2.3	4.4 ± 1.2	3.5 ± 2.3	6.8 ± 1.8

Table 2 Coordinates of the defect location as well as its length and width for different defect sizes. Reading from top to bottom: expected value (orange), experimental result (red) and FEM simulation result (blue).

Applying the lessons learned from papers I to III we focused on the case of the human eye. Due to the physiological similarities between porcine and human eyes [49], we selected porcine eyes to explore an alternative method to rebound tonometry.

The TA01 iCare rebound tonometer and a CMOP helped us visualize the dependence of the guided wave velocity on pressure (Fig. 16). A pressure series, where we cycled the IOP from 15 to 40 mmHg with a porcine eye, established the repeatability of our method on an eye (Fig. 17). We further consolidated the validity of the approach by measuring multiple eyes and comparing the results to those obtained from the CMOP experiments (Fig. 18).

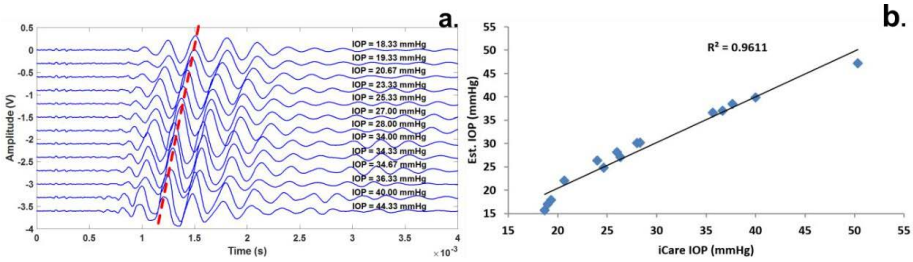

Figure 16 Validation of the method using an ocular phantom. Left: we arbitrarily chose the third peak of the waveform to estimate the time-of-arrival as a function of IOP. Right: Calibration curve relating the estimated IOP to the readings from the iCare TA01 tonometer.

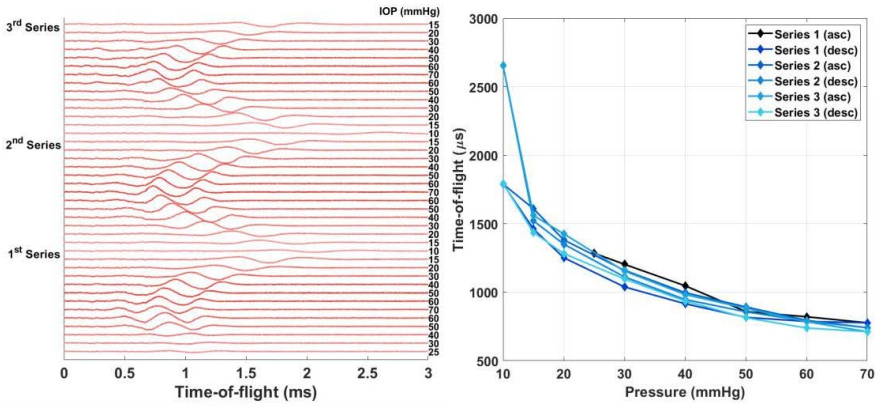

Figure 17 Pressure sweeps within a porcine eye. Left: visualization of the time dependence of guided waves on IOP. Right: time-of-flight of the guided waves as a function of IOP. Low IOP feature higher sensitivity than high pressures.

The calibration curve for our contactless tonometer is the result of fitting a power function to the experimental data. This choice of function is not derived from theory but motivated by the data extracted from experiments with porcine eyes (Fig. 18A). We further processed data from these experiments by characterizing the discrepancy of the IOPs predicted by our calibration curve and the absolute pressure measurements obtained from the water-column manometer (Fig. 18B & 18C).

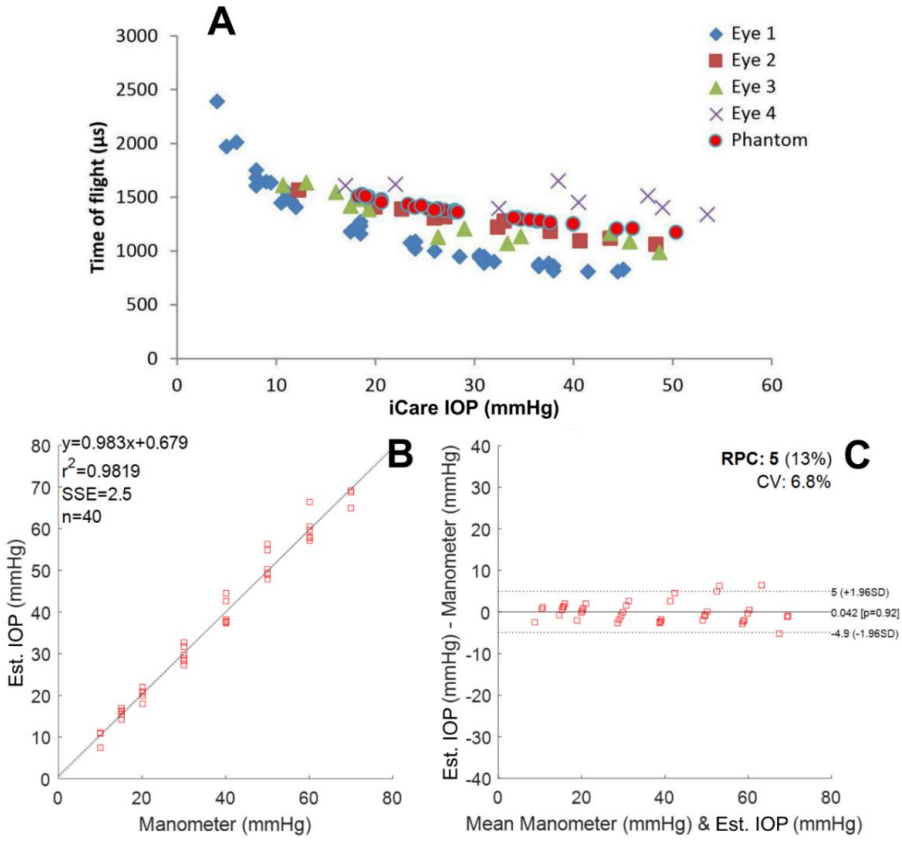

Figure 18 Comparison of the time-of-flight of guided waves travelling on the surface of porcine eyes (a) and on an ocular phantom (b). Estimated IOP for porcine eyes using our approach compared to the readings from a water-column manometer. C. Bland-Altman plot showing the discrepancy between the obtained values using our approach and the water-column manometer results.

4 Discussion

The development of the laser-based tonometer rests on the foundation laid by publications I to IV. Focusing acoustic power with a metamaterial lens (Fig 7 and Fig 8) allows localized actuation with a footprint smaller than the central wavelength. The wide bandwidth shock wave excitation could unfortunately not be effectively focused with such a metamaterial lens. The filling of the lens as well as its dimensions have been chosen to effectively focus a narrow range of frequencies (Fig. 7 and Fig. 9). Nevertheless, the idea behind publication I of generating an acoustic sheet could excite an acoustic line source on the surface of the eye by means of laser ablation. Because of viscous damping, acoustic resonances are not an issue as it is in publication III however acoustic attenuation is. Acoustic line sources feature lower geometric attenuation leading to higher signal-to-noise ratio which is low for laser interferometry as compared to contacting techniques.

Returning to the matter of membrane wave excitation, the wide-bandwidth shock excitation was instead localized with an aluminum plate featuring a 2 mm hole. The presence of the hole restricts the footprint of the excitation to a small region on the surface of the eye (or phantom), launching membrane waves. The time-of-flight of the membrane waves allows the calculation of the IOP, and the aluminum plate ensures that the membrane wave excitation is localized on the periphery of the eye. Such a region is comparable in size to the central wavelength of the acoustic wave package. As learned from paper III, when the wavelength is an order of magnitude larger than the radius of the sphere (eye) and one can ignore curvature-induced dispersion. Therefore, it is possible to treat the membrane waves as leaky Lamb waves where not only does the membrane stiffness have an impact on the waves velocity, but also the membrane (corneal) thickness (paper II and paper IV).

As shown by Hon [50], the corneal stiffness is dependent on IOP but not on central corneal thickness. The membrane wave velocity depends on both the corneal stiffness and the central corneal thickness. Since the corneal stiffness in a healthy eye is primarily a function of IOP, the wave velocity depends on the IOP and the corneal thickness. Future development of the contactless tonometer would benefit from corneal thickness measurements. This way it would be possible to compensate for the effect of corneal thickness variation

to reduce IOP uncertainty. It is possible than an above-the-average IOP would be measured as normal if the corneal thickness is thin. The high IOP speeds up the propagation of the membrane wave, but the thin cornea slows it down by the same amount.

The eye measurements use the same interferometric technology as in the propeller (paper II) and metal hemisphere (paper III) studies. In the propeller study we localized damage on a rotating aluminum blade (Fig. 10, Fig. 11) using a stroboscopic approach. The approach required precise timing of the excitation laser to generate guided waves at the desired locations on the rotating sample. Similarly, when measuring a patient, it is critical to ensure that the position of the eye is the same in every measurement to obtain consistent IOP readings. IOP uncertainty magnified by the arrangement of collagen fibrils [59]–[61] that are anisotropically distributed across the cornea [62]. As a result, the propagation velocity of guided waves varies along different propagation paths resulting in uncertain IOP values. To reduce IOP uncertainty it would be beneficial to map the elastic properties of the cornea. Perhaps a ray tracing approach such as the one suggested in paper II in combination with a directed acoustic source (paper III) would allow to launch acoustic waves in the cornea along directions of similar mechanical properties and reduce measurement uncertainty of the IOP values.

To assess the consistency of the results, we measured porcine eyes with a commercial IOP tonometer (icare TA01) designed for human use. We chose porcine eyes due to the physiological similarities between pig and humans (similar eye dimensions) and due to the availability of samples. Porcine eyes feature thicker cornea and diameter than human eyes. The thick cornea leads to faster membrane waves, but this effect is insignificant in comparison the increase in travel time of membrane waves due to the larger eye diameter. The large eye diameter leads to a long path between the membrane excitation and detection locations thus yielding a longer time-of-flight than in human studies.

We measured each porcine eyes in three pressure series where we increased, decreased and increased the pressure. The reason for this approach is that the tissue requires time to adapt to the changing pressure. The results (Fig. 17) show that the time-of-flight of the acoustic wave depends on the IOP. There is one outlier that shows a discrepancy of 300 μs, which corresponds to 1 mm travel distance on the surface of the eye. Such measurement discrepancy is likely due to the experimental nature of the setup (Fig. 18).

IOP measurements suffer from non-linearity of the sensitivity across the pressure range (Fig. 17 and Fig. 18). At low pressures (4-12 mmHg) the sensitivity is -123 μs mmHg-1 and at high pressures (31 to 38 mmHg) -18 μs mmHg-1. The reason for this sensitivity variation is the fact that the dependence of corneal elasticity on IOP is non-linear [51]. The corneal stiffness increases rapidly from 12 to 20 mmHg after which the stiffness gradually increases up to 60 mmHg [50]. The effect at high IOPs of the decrease in sensitivity increases measurement scatter as shown in the Bland-Altman plot (Fig. 18). The scatter results from systematic measurement errors that introduce variations in the distance that the acoustic wave travels from the excitation to the detection locations. As a result, at high IOPs a small difference in the time-of-flight of the acoustic wave leads to a large IOP error.

IOP values are directly calculated from the time-of-flight of membrane waves and one of the major sources of error is the LDV alignment. As learned from the study of hemispheres (paper III), even a small difference in the path length of the guided waves introduces a significant error in the IOP estimation. Since the LDV is an interferometer, the best signal-to-noise ratio is obtained when the distance from the measurement unit to the sample is a multiple of twice the laser cavity length [14]. The shortest optimum distance from the LDV laser head to the surface of the hemisphere is 232 mm and a tilt of only 11.4' results in a 1 mm difference on the surface of the sample. In the case of an eye, such a misalignment would result in a time difference of 200 μs, thus yielding an error of 1.6 mmHg at low pressure and 11.1 mmHg at high pressure. Considering that a healthy human IOP ranges from 10 to 21 mmHg it is paramount that the laser is well aligned to produce clinically relevant results.

Another parameter affecting the measured IOP values is the effect of the membrane protruding due to the IOP. A worst-case calculation assuming 3 mm bulging of the membrane over the entire pressure range shows that the time-of-flight is increased by 8 μs. Even though this could be considered a source of uncertainty, it does not account for the 300 μs difference in the time-of-flight. This is further indication that the IOP modifies the propagation velocity of the membrane waves. The shortening of the time-of-flight is not a geometric phenomenon.

To further verify the experimental results, we studied non-linearity by comparing the contactless method to the best-in-class rebound tonometer (iCare TA01, paper IV). When measuring the ocular phantom, we obtained the internal pressure from the iCare TA01 and when measuring eyes, we obtained the pressure both with the iCare TA01 and with a water column. In the eye experiments, the fact that there was agreement between the results offered by

our method and the values shown by the TA01 is a testimony to the adequacy of the ocular phantom as an eye model (Fig. 18).

Two important differences between the ocular phantom and an eye are the variation in corneal thickness as well as the viscoelasticity of the cornea. The cornea is viscoelastic [51], and as a result, the elastic response is stiff for fast mechanical excitations [52], [53]. Since the momentum carried by a shock wave front is dependent on the energy that generated said shock [54], it is important to sustain consistent energy for every generated shock wave to guarantee identical pressure measurements. Future pressure measurements will benefit from compensating for the effect of corneal thickness. Guided waves propagating in the eye propagate at different speeds depending upon the corneal thickness with waves propagating slower for thin corneas. A thin cornea would yield slow membrane waves leading to IOP underestimation. Such a result could also be inferred from the dependency of guided wave speed on plate thickness (Fig. 12) from which we extracted the depth of the defect on paper II.

Future development of the laser-based tonometer into a medical device requires confinement of the shock wave excitation on the periphery of the eye. The eye should be in a similar orientation across measurements to allow gathering data thus reducing measurement uncertainty. Avoiding systematic measurement error due to misalignment of the LDV in combination with prior knowledge of cornea thickness would provide confidence on the calculated IOP values. Measurement of human IOP requires an alternative measurement laser to the LDV since the helium-neon laser is not eye-safe. With patient safety and comfort in mind, the development of the tonometer introduced in this study might provide a future alternative to Goldmann.

5 Conclusion

The contactless nature of laser interferometry as well as shock wave excitation, allows contactless generation and detection of elastic waves. These waves probe the mechanical properties of the sample where they propagate, in this case porcine eyes. As a result, it is possible to measure the intraocular pressure in a contactless manner. The data, in combination with the techniques and expertise developed from the supporting publications prove the claim of this work.

6 References

[1] Y.-C. Tham, X. Li, T. Y. Wong, H. A. Quigley, T. Aung, and C.-Y. Cheng, "Global Prevalence of Glaucoma and Projections of Glaucoma Burden through 2040," *Ophthalmology*, vol. 121, no. 11, pp. 2081–2090, Nov. 2014.

[2] C. E. Traverso *et al.*, "Direct costs of glaucoma and severity of the disease: a multinational long term study of resource utilisation in Europe," *Br. J. Ophthalmol.*, vol. 89, no. 10, pp. 1245–1249, Oct. 2005.

[3] M. A. Kass, "Standardizing the Measurement of Intraocular Pressure for Clinical Research: Guidelines from the Eye Care Technology Forum," *Ophthalmology*, vol. 103, no. 1, pp. 183–185, Jan. 1996.

[4] A. Kontiola, "A new electromechanical method for measuring intraocular pressure," *Doc. Ophthalmol.*, vol. 93, no. 3, pp. 265–276, Sep. 1997.

[5] A. I. Kontiola, "A new induction-based impact method for measuring intraocular pressure," *Acta Ophthalmol. Scand.*, vol. 78, no. 2, pp. 142–145, Apr. 2000.

[6] M. E. Iliev, D. Goldblum, K. Katsoulis, C. Amstutz, and B. Frueh, "Comparison of rebound tonometry with Goldmann applanation tonometry and correlation with central corneal thickness," *Br. J. Ophthalmol.*, vol. 90, no. 7, pp. 833–835, Jul. 2006.

[7] M. B. Shields, "The non-contact tonometer. Its value and limitations," *Surv. Ophthalmol.*, vol. 24, no. 4, pp. 211–219, 1980.

[8] Q. K. Farhood, "Comparative evaluation of intraocular pressure with an air-puff tonometer versus a Goldmann applanation tonometer," *Clin. Ophthalmol.*, vol. 7, no. 1, p. 23, Dec. 2013.

[9] J. M. Britt, B. C. Clifton, H. S. Barnebey, and R. P. Mills, "Microaerosol Formation in Noncontact 'Air-Puff' Tonometry," *Arch. Ophthalmol.*, vol. 109, no. 2, pp. 225–228, 1991.

[10] A. A. Maznev and O. B. Wright, "Upholding the diffraction limit in the focusing of light and sound," *Wave Motion*, vol. 68, pp. 182–189, Jan. 2017.

[11] Z. Chen, A. Taflove, and V. Backman, "Photonic nanojet enhancement of backscattering of light by nanoparticles: a potential novel visible-light ultramicroscopy technique," *Opt. Express*, vol. 12, no. 7, p. 1214, Apr. 2004.

[12] I. Kassamakov, S. Lecler, A. Nolvi, A. Leong-Hoï, P. Montgomery, and E. Hæggström, "3D Super-Resolution Optical Profiling Using Microsphere Enhanced Mirau Interferometry," *Sci. Rep.*, vol. 7, no. 1, p. 3683, Dec. 2017.

[13] N. Hosoya, A. Yoshinaga, A. Kanda, and I. Kajiwara, "Non-contact and non-destructive Lamb wave generation using laser-induced plasma shock wave," *Int. J. Mech. Sci.*, vol. 140, pp. 486–492, May 2018.

[14] C.B Scruby and L.E Drain, *Laser ultrasonics, techniques and applications*, vol. 24, no. 3. 2003.

[15] L. Torrisi, A. Borrielli, and D. Margarone, "Study on the ablation threshold induced by pulsed lasers at different wavelengths," *Nucl. Instruments Methods Phys. Res. Sect. B Beam Interact. with Mater.*

Atoms, vol. 255, no. 2, pp. 373–379, Feb. 2007.
[16] N. Hosoya, I. Kajiwara, and T. Hosokawa, "Vibration testing based on impulse response excited by pulsed-laser ablation: Measurement of frequency response function with detection-free input," *J. Sound Vib.*, vol. 331, no. 6, pp. 1355–1365, Mar. 2012.
[17] F. Huda, I. Kajiwara, N. Hosoya, and S. Kawamura, "Bolt loosening analysis and diagnosis by non-contact laser excitation vibration tests," *Mech. Syst. Signal Process.*, vol. 40, no. 2, pp. 589–604, Nov. 2013.
[18] N. Hosoya, I. Kajiwara, K. Umenai, and S. Maeda, "Dynamic characterizations of underwater structures using noncontact vibration tests based on nanosecond laser ablation in water: evaluation of passive vibration suppression with damping materials," *JVC/Journal Vib. Control*, vol. 24, no. 16, pp. 3714–3725, Aug. 2018.
[19] N. Hosoya, R. Umino, I. Kajiwara, S. Maeda, T. Onuma, and A. Mihara, "Damage Detection in Transparent Materials Using Non-Contact Laser Excitation by Nano-Second Laser Ablation and High-Speed Polarization-imaging Camera," *Exp. Mech.*, vol. 56, no. 2, pp. 339–343, Feb. 2016.
[20] N. Hosoya, Y. Terashima, K. Umenai, and S. Maeda, "High spatial and temporal resolution measurement of mechanical properties in hydrogels by non-contact laser excitation," *AIP Adv.*, vol. 6, no. 9, Sep. 2016.
[21] N. Hosoya, R. Umino, A. Kanda, I. Kajiwara, and A. Yoshinaga, "Lamb wave generation using nanosecond laser ablation to detect damage," *JVC/Journal Vib. Control*, vol. 24, no. 24, pp. 5842–5853, Dec. 2018.
[22] N. Hosoya, I. Kajiwara, T. Inoue, and K. Umenai, "Non-contact acoustic tests based on nanosecond laser ablation: Generation of a pulse sound source with a small amplitude," *J. Sound Vib.*, vol. 333, no. 18, pp. 4254–4264, Sep. 2014.
[23] Y. Shui, D. Royer, E. Dieulesaint, and Z. Sun, "Resonance of surface waves on spheres," in *Ultrasonics Symposium Proceedings*, 1988, vol. 1, pp. 343–346.
[24] D. Veira Canle, J. Mäkinen, R. Blomqvist, M. Gritsevich, A. Salmi, and E. Hæggström, "Defect localization by an extended laser source on a hemisphere," *Sci. Reports 2021 111*, vol. 11, no. 1, pp. 1–7, Jul. 2021.
[25] M. C. Junger, "Sound Scattering by Thin Elastic Shells," *J. Acoust. Soc. Am.*, vol. 24, no. 4, pp. 366–373, Jul. 1952.
[26] C. Y. Tsui, G. N. Reid, and G. C. Gaunaurd, "Resonance scattering by elastic cylinders and their experimental verification," *J. Acoust. Soc. Am.*, vol. 80, no. 2, pp. 382–390, Aug. 1986.
[27] D. A. Hutchins, R. J. Dewhurst, and S. B. Palmer, "Directivity patterns of laser-generated ultrasound in aluminum," *Cit. J. Acoust. Soc. Am.*, vol. 70, p. 1362, 1981.
[28] A. M. Aindow, R. J. Dewhurst, and S. B. Palmer, "Laser-generation of directional surface acoustic wave pulses in metals," *Opt. Commun.*, vol. 42, no. 2, pp. 116–120, Jun. 1982.
[29] H. Kim, K. Jhang, M. Shin, and J. Kim, "A noncontact NDE method using a laser generated focused-Lamb wave with enhanced defect-detection ability and spatial resolution," *NDT E Int.*, vol. 39, no. 4, pp. 312–319, Jun. 2006.

[30] A. D. W. McKie, J. W. Wagner, J. B. Spicer, and C. M. Penney, “Laser generation of narrow-band and directed ultrasound,” *Ultrasonics*, vol. 27, no. 6, pp. 323–330, Nov. 1989.
[31] N. (Nicholas A. Brigman, “Structural health monitoring in commercial aviation,” 2012.
[32] “Nondestructive Evaluation Techniques : Thermography.” [Online]. Available: https://www.nde-ed.org/NDETechniques/Thermography/IR_Intro.xhtml. [Accessed: 18-Apr-2022].
[33] E. Z. Kordatos, D. G. Aggelis, and T. E. Matikas, “Monitoring mechanical damage in structural materials using complimentary NDE techniques based on thermography and acoustic emission,” *Compos. Part B Eng.*, vol. 43, no. 6, pp. 2676–2686, Sep. 2012.
[34] Q. Yu, O. Obeidat, and X. Han, “Ultrasound wave excitation in thermal NDE for defect detection,” *NDT E Int.*, vol. 100, pp. 153–165, Dec. 2018.
[35] J. M. Buckley, “An introduction to Eddy Current Testing theory and technology.”
[36] R. Smith, “Deep corrosion and crack detection in aging aircraft using transient eddy-current NDE,” 1999.
[37] “Crack Depth Measurement using Eddy-Current NDE.” [Online]. Available: https://www.ndt.net/apcndt2001/papers/1032/1032.htm. [Accessed: 18-Apr-2022].
[38] G. Y. Tian, Y. He, I. Adewale, and A. Simm, “Research on spectral response of pulsed eddy current and NDE applications,” *Sensors Actuators, A Phys.*, vol. 189, pp. 313–320, 2013.
[39] I. Mohanty, R. Nagendran, A. V. Thanikai Arasu, R. Baskaran, and A. Mani, “Correlation of defect depth with diffusion time of eddy currents for the defects in conducting materials using transient eddy current NDE,” *Meas. Sci. Technol.*, vol. 29, no. 10, Aug. 2018.
[40] I. Pelivanov *et al.*, “High resolution imaging of impacted CFRP composites with a fiber-optic laser-ultrasound scanner,” *Photoacoustics*, vol. 4, no. 2, pp. 55–64, Jun. 2016.
[41] E. R. Burke, V. Grubsky, V. Romanov, and K. Shoemaker, “NDE of spacecraft materials using 3D Compton backscatter x-ray imaging,” *AIP Conf. Proc.*, vol. 1706, Feb. 2016.
[42] A. Thompson, I. Maskery, and R. K. Leach, “X-ray computed tomography for additive manufacturing: A review,” *Meas. Sci. Technol.*, vol. 27, no. 7, Jun. 2016.
[43] C. L. Moore and J. A. Copel, “Current concepts: Point-of-care ultrasonography,” *N. Engl. J. Med.*, vol. 364, no. 8, 2011.
[44] C. Rajani, A. Klami, A. Salmi, T. Rauhala, E. Haggstrom, and P. Myllymaki, “Detecting industrial fouling by monotonicity during ultrasonic cleaning,” *IEEE Int. Work. Mach. Learn. Signal Process. MLSP*, vol. 2018-September, Oct. 2018.
[45] C. J. Todaro *et al.*, “Grain structure control during metal 3D printing by high-intensity ultrasound,” *Nat. Commun. 2020 111*, vol. 11, no. 1, pp. 1–9, Jan. 2020.
[46] Ł. Ambroziński *et al.*, “Acoustic micro-tapping for non-contact 4D imaging of tissue elasticity,” *Sci. Rep.*, vol. 6, no. 1, p. 38967, Dec. 2016.
[47] H. Balamane, T. Halicioglu, and W. A. Tiller, “Comparative study of

silicon empirical interatomic potentials," *Phys. Rev. B. Condens. Matter*, vol. 46, no. 4, pp. 2250–2279, 1992.
[48] M. Laradji, D. P. Landau, and B. Dunweg, "A Monte Carlo Simulation of the Stillinger-Weber Model for Si-Ge Alloys," *MRS Online Proc. Libr.*, vol. 358, pp. 67–72, 1994.
[49] J. Ruiz-Ederra *et al.*, "The pig eye as a novel model of glaucoma," *Exp. Eye Res.*, vol. 81, no. 5, pp. 561–569, Nov. 2005.
[50] Y. Hon, G.-Z. Chen, S.-H. Lu, D. C. Lam, and A. K. Lam, "In vivo measurement of regional corneal tangent modulus," *Sci. Rep.*, vol. 7, no. 1, p. 14974, Dec. 2017.
[51] C. J. Roberts, "Concepts and misconceptions in corneal biomechanics," *J. Cataract Refract. Surg.*, vol. 40, no. 6, pp. 862–869, 2014.
[52] A. Elsheikh, D. Wang, M. Brown, P. Rama, M. Campanelli, and D. Pye, "Assessment of corneal biomechanical properties and their variation with age," *Curr. Eye Res.*, vol. 32, no. 1, pp. 11–19, Jan. 2007.
[53] A. Elsheikh, D. Wang, P. Rama, M. Campanelli, and D. Garway-Heath, "Experimental assessment of human corneal hysteresis," *Curr. Eye Res.*, vol. 33, no. 3, pp. 205–213, 2008.
[54] L. D. Landau and E. M. Lifshitz, *Fluid Mechanics, Course on Theoretical Physics*, vol. 6. Oxford: Pergamon Press, 1959.

Appendix A: Defect reconstruction on planar and curved geometries

To determine the dimensions of the scatterer in the propeller case (paper II), we first calculate the phase and group velocity of the guided waves. Calculating the group velocity of the antisymmetric mode is possible by measuring the distance between the excitation and the detection point, as well as the time-of-arrival of the mode (Fig. 11). The phase velocity, however, has been calculated from the time that it takes a given part of the antisymmetric wave front to interact with the defect, in other words, a part of the wave travelling with a given phase.

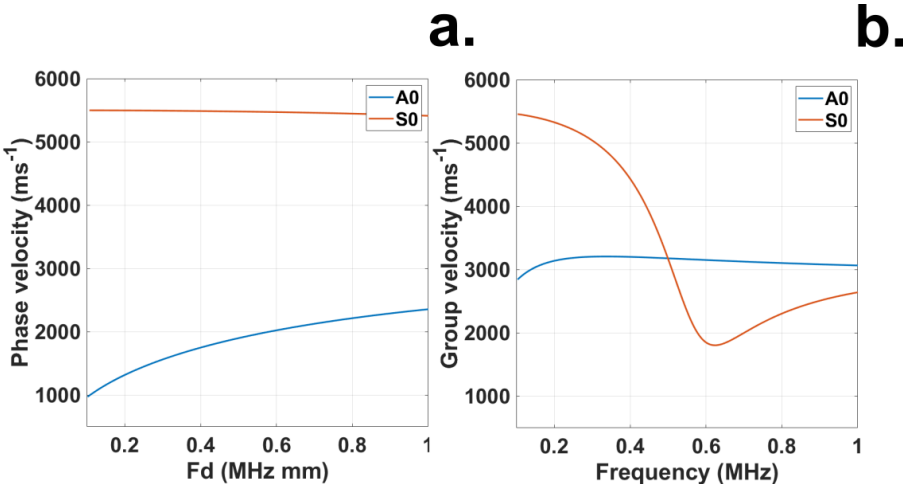

Figure 19 Lamb wave theoretical dispersion curves: Group velocity as a function of frequency for a 4 mm thick aluminum plate (a). Phase velocity over frequency times thickness product for an aluminum plate (b).

The group velocity in the undamaged region of the blade for the antisymmetric mode is $v_g = (3180 \pm 32)\ ms^{-1}$ and the phase velocity in the damaged region $v_2 = (1686 \pm 371)\ ms^{-1}$. From the corresponding dispersion curve (Fig. 19A) the central frequency turns out to be $f = (0.209 \pm 0.024)$ MHz From the measured phase velocity in the damaged region one can calculate the thickness times frequency product as $Fd = (0.366 \pm 0.208)$ MHz mm.

The thickness of the damaged region is then calculated as $T = \frac{Fd}{f} = (1.7 \pm 1.0)$ mm. Since the plate thickness is 4 mm, the depth of the notch is $D = (2.3 \pm 1.0)$ mm.

The reconstruction of a 3D model of a hemisphere with defects requires to know their exact location and dimensions. We first estimated the location by calculating the group velocity of the A_0 mode. The group velocity is simply the arc length from the excitation to the detection location (d) divided by the travel time of the acoustic wave (t, Eq. 1). We defined the travel time as the time difference between the firing of the excitation laser and the first peak of the travelling wave form (Fig. 15C, 5F).

$$v_{A_0} = \frac{d}{t} = \frac{1}{t}\left(\frac{\pi}{2}R - 0.85\ \text{mm}\right) = (3056 \pm 120)\ \text{ms}^{-1} \quad (1)$$

Where R is the radius of the hemisphere and 0.85 mm is the distance from the equator to the detection point. The standard deviation for all the figures features confidence limits of one standard deviation.

If we approximate the footprint of the defect to be square, we can calculate the width (w) and the length (l) of the defect from (Eq. 2, Fig. 20):

$$w = l = \alpha R = R\,\text{atan}\left(\frac{d}{2R}\right) \quad \alpha = \text{atan}\left(\frac{d}{2R}\right) \quad (2)$$

here d is drill bit diameter used to perforate the shell and α the angle encompassing the size of the defect. Considering that we used a stand to drill the defect at a polar angle of $\theta = 45^{o}$, the polar angles defining the defect are $\theta_{1,2} = 45° \pm \frac{\alpha}{2}$. Similarly, we arbitrarily selected an azimuth $\phi = 121°$, thus the estimated azimuthal coordinates are $\phi_{1,2} = 121 \pm \frac{\alpha}{2}$.

From the laser ultrasound experiments, we determined the azimuthal boundaries of the defect from the drop in the acoustic power that is shadowed by the defect (Eq. 3).

$$P\ \alpha\ \frac{\int_{t_1}^{t_2} A(t)^2 dt}{\int_{t_1}^{t_2} dt} \quad \text{where} \quad t_1 = 10\ \mu s \ \text{ and } \ t_2 = 20\ \mu s \quad (3)$$

Where P represents the acoustic power and A the acoustic wave amplitude.

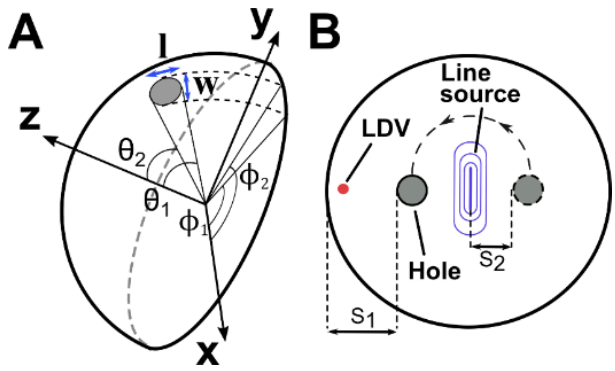

Figure 20 Defect coordinates and dimensions. In practice, we assume that a square sector delimited by angles ϕ_1, ϕ_2 and θ_1, θ_2 contains the defect (a, grey disk). We calculate its dimensions (width w, and length l) by studying the shadowing of the acoustic wave form by the defect as well as the echoes that are reflected from said scatterer (b).

Considering that the acoustic power is proportional to the amplitude of the propagating wave form squared, the -3 dB roll-off points correspond to ϕ_1 and ϕ_2. It is straightforward to convert from these azimuthal coordinates to the defect width (Eq.4):

$$w = R\,(\phi_2 - \phi_1) \quad (4)$$

The defect length (l) requires interpretation of the ballistic wave form and its echo. By measuring the time difference between the ballistic A_0 mode and the arrival of the echoes reflected by the defect (both in direct line-of-sight and in the antipodal location), $\Delta t_1$and Δt_2 respectively, one can calculate the polar angles θ_1 and θ_2 and infer the defect length l (Eq. 5):

$$s_{1,2} = \frac{\Delta t_{1,2}}{2} v_{A_0} \quad \theta_1 = \frac{1}{R} s_1 \quad \theta_2 = \frac{\pi}{2} - \frac{1}{R} s_2 \quad (5)$$
$$l = \frac{\pi}{2} R - s_1 - s_2$$

In addition to the dimensions of the defect, we evaluated the efficacy of the extended laser source for generating directed acoustic waves. Directivity is the dominant direction of the flow of energy. The visualization of the acoustic power (Eq. 3) allows to compare the difference in the acoustic field directivity produced by a point and a line source (Fig. 21). To generate the point source acoustic maps, we focused the Nd: YAG laser with a spherical lens into a spot (Ø=1 mm) at the apex of the shell (Fig.2B). Similarly, a cylindrical lens generated a line (7.8 mm long, 0.8 mm wide) launching acoustic waves with an energy profile reaching a maximum perpendicular to the longitudinal axis of the line. To be able to probe the line we held the cylindrical lens with an adaptor featuring windows allowing the LDV to scan the acoustic field along the equator of the hemisphere.

FEM simulations verified the experimental results whilst benefiting from the symmetry of the sample and the setup. To simulate a rotating line source, we placed two detection locations that measured the out-of-plane displacement along the meridian and simulated a 90° rotation. Mirroring the simulation results provides a complete 360° map of the acoustic wave amplitude (Fig 21).

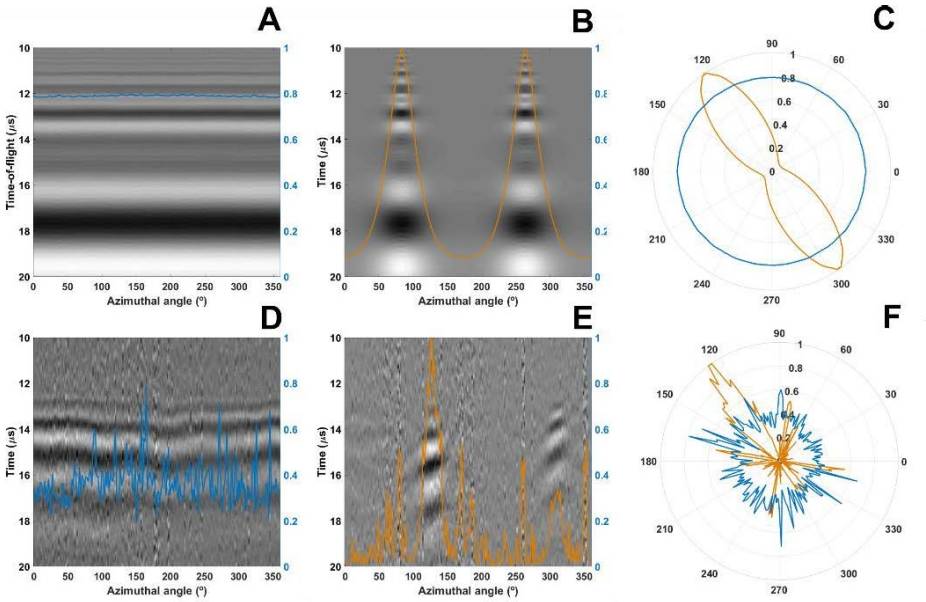

Figure 21 Directivity studies featuring a point and a line acoustic source. Comparison of FEM simulations (top row) and experimental results (bottom row). The first column corresponds to a point source, the second to a line source and the third column contains the acoustic power directivity plots. The blue and orange solid lines correspond to the acoustic power (Eq. 3) normalized to the maximum of the acoustic power generated by the line source for that case (simulation or experimental).

Appendix B: Uncertainty calculations

For the quantities corresponding to the propeller case (paper II), since every experiment was repeated three times, the calculated parameters were averaged. Their uncertainty was estimated as:

$$S(x) = \sqrt{S_A(x) + S_B(x)} \quad (6)$$

S(x) is the uncertainty of the x parameter, $S_A(x)$ the standard deviation of the mean, and $S_B(x)$ the empirical uncertainty estimate.

For the linear fit to calculate the group velocity of the A_0 mode (Fig. 11) the uncertainty in the time of flight was estimated to be $S_B(t) = 0.58\ \mu s$. This uncertainty was derived from the rise time of the A_0 wave front.

$$S_B(v_G) = \frac{S(b)}{b^2} \quad (7)$$

Here b is the slope of the linear fit to the experimental data whereas $S_B(v_G)$ is the uncertainty in group velocity.

The uncertainty in notch length $S_B(a)$ is estimated as the thickness of the lines (Fig. 11) that indicate wave reflection, to be 0.75 mm.

The uncertainty in distance from the center of the sample to the edge of the notch was estimated by propagation of uncertainty.

$$S_B(d) = \sqrt{t^2 S^2(v_g) + v_g^2 S^2(t)} \quad (8)$$

Here t is the time of arrival of the reflected A_0 mode and S(t) is its time uncertainty.

The uncertainty in frequency $S_B(f)$ was calculated from the theoretical dispersion curves by subtracting the corresponding frequencies to $v_1 - S(v_1)$ and $v_1 + S(v_1)$. For the notched part of the sample, the uncertainty in the fd product, $S_B(fd)$, was computed in a similar way, this time by subtracting the corresponding fd products for $v_2 - S(v_2)$ and $v_2 + S(v_2)$. Next the uncertainty in notch depth was estimated as:

$$S_B(D) = \frac{\sqrt{S^2(fd)+S^2(f)D^2}}{f} \quad (9)$$

From Eq.7 one can use propagation of uncertainties to show that the uncertainty in A_0 group velocity is:

$$S_B(v_2) = \sqrt{\left(\frac{\partial v_2}{\partial R}S(R)\right)^2 + \left(\frac{\partial v_2}{\partial t}S(t)\right)^2 + \left(\frac{\partial v_2}{\partial v_1}S(v_1)\right)^2 + \left(\frac{\partial v_2}{\partial d}S(d)\right)^2} \quad (10)$$

$$\frac{\partial v_2}{\partial R} = \frac{t-\frac{d}{v_1}}{\left(t-\frac{d-R}{v_1}\right)^2} \quad (11) \qquad \frac{\partial v_2}{\partial t} = -\frac{R}{\left(t-\frac{d-R}{v_1}\right)} \quad (12) \qquad \frac{\partial v_2}{\partial v_1} = \frac{\frac{R(d-R)}{v_1^2}}{\left(t-\frac{d-R}{v_1}\right)} \quad (13)$$

$$\frac{\partial v_2}{\partial d} = \frac{\frac{R}{v_1}}{\left(t-\frac{d-R}{v_1}\right)^2} \quad (14)$$

In the hemisphere study (paper III), the distance from the LDV detection location to the edge (equator) of the sample, as well as the sample thickness and diameter was measured with a digital calliper and we estimate the measurement error as 0.05 mm, i.e., the resolution of the calliper.

The group velocity of the A_0 mode used for the reconstruction of the defect features a standard deviation (Eq. 15):

$$S(v_{A_0}) = \frac{1}{t}\sqrt{S^2(d) + v^2S^2(t)} \quad S(t) = \sqrt{S^2(t_{exp}) + S^2(t_{av})} \quad (15)$$

$S^2(d)$ and $S^2(t)$ are variance in distance travelled by the guided wave and travel time, respectively. Since we average the acoustic signals over several rotations, we calculated the uncertainty in the time-of-flight as a combination of $S(t_{exp})$, i.e., the time difference between the first and the second wave crests of the A_0 wave front and $S(t_{av})$, the standard deviation of the mean.

Propagating uncertainties, we estimated the standard deviation of the polar angles $S(\theta)$ as (Eq. 16):

$$S(\Theta) = \frac{1}{D}\sqrt{v_{A_0}^2S^2(\Delta t) + \Delta t^2S^2(v_{A_0}) + \Theta^2S^2(D)} \quad (16)$$

Contributing factors to the polar angle uncertainty are the variance of the time difference between the arrival of the ballistic wave and the echo reflected by the defect $S^2(\Delta t)$ as well as the variance of the sample diamter $S^2(D)$.

The defect length features a standard deviation (Eq. 17):

$$S(l) = \sqrt{S^2(s_T) + S^2(s_1) + S^2(s_2)} = \sqrt{S^2(s_T) + 2S^2(s)} \quad (17)$$

Finally, the width of the defect features a standard deviation that is derived from the shadowing of the acoustic power. Propagation of uncertainties applied to Eq.2 yields (Eq. 18):

$$S(w) = \sqrt{(\Delta\phi)^2 S^2(R) + R^2 S^2(\Delta\phi)} \quad (18)$$